

# Fracture Toughness of $\text{Co}_4\text{Sb}_{12}$ and $\text{In}_{0.1}\text{Co}_4\text{Sb}_{12}$ Thermoelectric Skutterudites Evaluated by Three Methods

*James Eilertsen<sup>a, b, 1</sup>, M. A. Subramanian<sup>a</sup>, J. J. Kruzic<sup>b, \*</sup>*

<sup>a</sup>Department of Chemistry, Oregon State University, Corvallis, OR 97331, USA

<sup>b</sup>School of Mechanical, Industrial, and Manufacturing Engineering, Oregon State University, Corvallis, OR 97331, USA

## Abstract

Interstitially filled skutterudites are a promising class of state-of-the-art thermoelectric materials. Although thermoelectrics are exposed to significant thermal stresses, little information is known about the fracture toughness of interstitially doped skutterudites. This work explores the fracture toughness of undoped  $\text{Co}_4\text{Sb}_{12}$  and indium doped  $\text{In}_{0.1}\text{Co}_4\text{Sb}_{12}$  skutterudites using three methods: 1) Vickers indentation fracture (VIF), 2) Vickers indent crack opening displacement (COD), and 3) single-edge vee-notched bend (SEVNB) in 4-point flexure. Indium addition to the icosahedral void-sites is verified by an observed increase in the crystal lattice parameter and strongly enhanced thermoelectric properties in the indium-doped samples. Fracture toughness values for  $\text{Co}_4\text{Sb}_{12}$  and interstitially doped  $\text{In}_{0.1}\text{Co}_4\text{Sb}_{12}$  were found to be identical using both the COD and SEVNB methods indicating no interstitial embrittlement occurs due to indium void-site filling. Furthermore, it was found that there is no significant extrinsic toughening by crack bridging or other mechanisms and the toughness was insensitive to grain size variations. Fracture toughness values derived from the Vickers indentation fracture (VIF) method did not agree with the other two methods and it is recommended that that method be avoided. The results indicate that the fracture toughness of skutterudites may be, at least in some cases, significantly lower ( $\sim 0.5 \text{ MPa}\sqrt{\text{m}}$ ) than previously reported and there may be concern over the durability of skutterudite-based power-producing thermoelectric modules if care is not taken to ensure adequate toughness.

**Keywords:** Thermoelectric Materials, Mechanical Properties, Fracture Toughness, Skutterudites, Interstitially Doped Semiconductors

---

\*Corresponding author. Tel.: +1 541 7377027; fax: +1 541 7372600

E-mail address: [jamie.kruzic@oregonstate.edu](mailto:jamie.kruzic@oregonstate.edu) (J. J. Kruzic)

<sup>1</sup> Present Address: EMPA, Solid State Chemistry and Catalysis, Ueberlandstrasse 129, CH-8600 Duebendorf, Switzerland

## 1. Introduction

There is a current demand for a diverse array of clean and sustainable energy technologies. This demand may be met in part by high-efficiency thermoelectric materials [1, 2]. Thermoelectric materials are solid-state semiconductors that generate an electric potential when subjected to a thermal gradient. A thermoelectric module, essentially a collection of thermoelectric materials connected in series by metal contacts and dimensionally restrained by ceramic dielectrics [1], can produce emission-free electric power continuously when a thermal gradient is sustained [3].

Maximum efficiency ( $\phi_{max}$ ) is strongly dependent on the operating conditions; namely, the thermal gradient ( $T_1-T_2$ ), the average operating temperature ( $T$ ), and the intrinsic transport properties (reflected in  $Z$ ) of the thermoelectric material:

$$\phi_{max} = \left( \frac{T_1 - T_2}{T_1} \right) \left( \frac{\sqrt{1+ZT} - 1}{\sqrt{1+ZT} + \frac{T_2}{T_1}} \right) \quad (1)$$

$Z$  is the material-dependent thermoelectric figure of merit, the widely used indicator for assessing the viability of thermoelectric materials, and it is usually formulated as a dimensionless figure-of-merit ( $ZT$ ) at a specified temperature:

$$ZT = \frac{S^2 \sigma}{\kappa_T} T \quad (2)$$

where the Seebeck coefficient ( $S$ ), the electrical conductivity ( $\sigma$ ), and the total thermal conductivity ( $\kappa_T$ ), are intrinsic material properties [4]. Consequently, maximum efficiency is obtained when the thermoelectric materials are subjected to the greatest possible temperature gradient, the highest operating temperature, and when they possess high electrical conductivity, low thermal conductivity, and a large Seebeck coefficient [5].

Skutterudites are a particularly promising class of thermoelectric materials as their thermoelectric properties can be tuned easily, resulting in some of the highest ZT values observed in single-phase materials [3, 6]. This tuning is achieved in skutterudites by utilizing their unusual cage-like crystal structure, which consist of two large icosahedral void-sites per unit cell. The reader should refer to [7, 8] for more details on the structure, but in short the icosahedral void-sites can expand to accommodate a wide-variety of disparate elements ranging from the alkalis, alkaline earths, and rare earths, to a number of poor metals and semimetals including indium, germanium, tin, and thallium [3, 9-13]. Furthermore, a sizable increase in ZT is often exhibited for interstitially doped skutterudites compared to their undoped counterparts [3, 12, 14, 15].

Interstitial substitutions, however, often lead to embrittlement in metals and intermetallics. This may be a concern for thermoelectric skutterudites as the combination of thermal gradients and dimensional constraint by dielectric ceramic materials induces significant stresses in power-generating thermoelectric modules. Mechanisms such as dislocation pinning [16], grain boundary embrittlement [17, 18], and a fundamental decrease in bond strength due to the interstitial [19, 20] all have been reported to enhance brittle fracture of many interstitially doped materials. The latter two may be relevant to brittle skutterudites.

Grain boundary embrittlement due to the precipitation of metastable void-site interstitial fillers is a potential concern as many filled skutterudites are interstitially doped with filling elements that are known (i.e. indium) or theorized to be metastable (i.e. thallium, tin, gallium, germanium, lead) [7, 8, 14, 21, 22]. It is conceivable that metastable interstitials may diffuse through the large cage-like skutterudite crystal structure to precipitate at grain boundaries. Even without precipitation, another potential grain boundary embrittlement mechanism is reduced bond strength at the grain boundaries due to the segregated dopants. For example, Messmer and Briant [19] associated enhanced intergranular embrittlement of Fe and Ni with a reduction in metal-metal bond strength in the vicinity of segregated sulfur near grain boundaries. Although skutterudites are intermetallic materials, an analogous effect may be possible in interstitially doped compositions. Finally, easier cleavage fracture and lower toughness is possible due to reduced bond strength within the grains. Electronic dispersion computations performed by Wee et al. [23] for  $\text{Co}_4\text{Sb}_{12}$  and barium-filled  $\text{Co}_4\text{Sb}_{12}$  skutterudites exhibit substantial bonding and antibonding character at the Brillouin Zone center in the highest valence and lowest conduction bands, respectively. Consequently, an increase in the lattice parameter, as observed in the interstitially doped antimonide skutterudites, should weaken the covalent bonding interaction, resulting in diminished bond strength and potentially leading to reduced fracture toughness.

Although a study by Ravi et al. [24] and an extensive review by Rogl and Rogl [25] have reported the mechanical properties of many skutterudites, neither compared the fracture toughness of un-doped and doped (filled) skutterudites with the same transition metal pnictogen void-site framework. To the authors' knowledge, no research has been published that focuses specifically on determining the effect of the interstitial on the fracture toughness of filled skutterudites. Moreover, much of the fracture toughness data that has been published [25] is derived from measuring crack lengths emanating from Vickers hardness indentations using the Vickers Indent Fracture (VIF) technique developed by Anstis et al. [26]. A number of publications, however, have definitively shown the inaccuracy of this technique [27-34].

Conversely, methods measuring the crack opening displacements (CODs) of Vickers indent cracks [35-41], or those using bend beams with sharp vee-shaped notches [30, 42-46], have been shown to be much more accurate for brittle materials. Accordingly, this study compares the fracture toughness of undoped and doped cobalt antimonide skutterudites determined from both Vickers indentation crack methods (VIF and COD) as well as using single-edge vee-notched bending (SEVNB) specimens.

## 2. Materials and Methods

### 2.1 Material Synthesis

$\text{Co}_4\text{Sb}_{12}$  and indium-filled  $\text{In}_{0.1}\text{Co}_4\text{Sb}_{12}$  compositions were chosen for this study. Although higher indium content skutterudites (up to  $\text{In}_{0.2}\text{Co}_4\text{Sb}_{12}$ ) show higher ZT values, they also show an InSb-impurity phase [47]. Focusing on  $\text{In}_{0.1}\text{Co}_4\text{Sb}_{12}$  was intended to ensure that only the effects of the void-site filler were examined.

The  $\text{Co}_4\text{Sb}_{12}$  and indium-filled  $\text{In}_{0.1}\text{Co}_4\text{Sb}_{12}$  compositions were synthesized according to a procedure developed by He et al. [12]. The as-synthesized powder was briefly ground in an agate mortar, divided, and loaded into 12 mm and 40 mm graphite dies. The 12 mm samples were hot pressed for 30 minutes with 200 MPa uniaxial pressure according to a procedure developed by the authors [7]. The 40 mm samples, however, were hot pressed for a longer duration (3 hours) at a lower pressure (50 MPa). The resulting 12 mm and 40 mm  $\text{Co}_4\text{Sb}_{12}$  and  $\text{In}_{0.1}\text{Co}_4\text{Sb}_{12}$  pellets were nearly 100% dense as determined by the Archimedes method.

### 2.2 Crystal- and Micro-structural Analysis

X-ray diffraction (XRD) data were collected on ground as-synthesized and post-sintered sample powders using a Rigaku Ultima IV Multipurpose X-ray Diffraction System. The samples were loaded onto an oriented Si single-crystal sample holder (MTI Corporation) with nearly zero background to maximize the possibility of detecting impurity phases. Diffraction patterns were collected with a fixed-time scan rate of  $0.01^\circ \text{step}^{-1}$  and  $0.1 \text{ sec step}^{-1}$  from  $2\theta = 10$  to  $120^\circ$ .

The diffraction data were analyzed using the Le Bail technique [48] as implemented in the Fullprof program [49]. Peak shape was described by a Pseudo-Voigt function with additional asymmetric parameters for low-angle domain peaks (below  $2\theta=40^\circ$ ), and the background level was fitted with a linear interpolation between a set of 40 to 60 given points with refinable heights.

Samples were prepared for microstructural analysis by grinding and polishing first with successively finer grades of SiC abrasive paper and then with abrasive alumina slurries. The samples were etched briefly (for 20 to 30 seconds) with freshly prepared aqua regia (1 part HNO<sub>3</sub>: 3 part HCl) and analyzed on using a Quanta 600F field emission scanning electron microscope (SEM) and Leica DMRM optical microscope. The average grain size of all samples was estimated using the Hilliard [50] intercept method conforming to the procedure outlined by ASTM E112-10 [51]. The average grain size is reported as the mean intercept length.

### 2.3 Thermoelectric Property Analysis

Electrical conductivity and Seebeck coefficient data were collected on 2 X 2 X 10 mm samples cut from the 12 mm and 40 mm sintered pellets with a low-speed, water-cooled diamond saw, and lightly polished with 1000-grit SiC sandpaper. The electrical conductivities and Seebeck coefficients were collected using an Ulvac-Riko ZEM 3 under static helium atmosphere from 300 to 600 K. The Ulvac-Riko ZEM 3 measures electrical conductivity and Seebeck coefficient nearly simultaneously using the linear 4-probe technique with altering polarity and the static DC method, respectively.

Thermal conductivity of the 12 mm samples was determined by measuring the thermal diffusivity ( $\alpha$ ) and specific heat ( $C_p$ ) data of both samples. Thermal conductivity data was not collected for the 40 mm samples; however, as the entire 40 mm pellet was used to machine large (3 X 4 X 25-31 mm<sup>3</sup>) bend beam fracture toughness specimens (Sec. 2.4). The data was collected under flowing N<sub>2</sub> using a Netzsch LFA 457 Micro Flash, and a Mettler Toledo 821e differential scanning calorimeter, respectively. Total thermal conductivity was determined from the relation  $\kappa_T = c_p \alpha d$ , where  $d$  is the sample bulk density.

### 2.4 Fracture Toughness Analysis

Vickers indentations and single-edge vee-notch bend (SEVNB) specimens in 4-point flexure were used to measure the fracture toughness of the 12 mm and 40 mm samples, respectively. In addition to the VIF method [26] for indentation fracture toughness, the intrinsic crack-tip toughness ( $K_{tip}$ ) was determined from the crack-tip opening displacements (CODs) of Vickers induced radial cracks. Indent forces were varied from a range of 4.9 to 9.8 N for Co<sub>4</sub>Sb<sub>12</sub> down to a range of 0.25 to 0.98 N for In<sub>0.1</sub>Co<sub>4</sub>Sb<sub>12</sub> to avoid lateral crack induced spalling.

The Vickers indent derived VIF fracture toughness ( $K_C$ ) was calculated from the applied indenter load ( $P$ ), Young's modulus ( $E$ ), hardness ( $H$ ), and mean radial crack length ( $c$ ) [26]:

$$K_C = \beta \left( \frac{E}{H} \right)^{0.5} \left( \frac{P}{c^{1.5}} \right) \quad (3)$$

where  $\beta$  is an empirical calibration constant taken to be 0.016, and  $E$  is taken to be equal to 140 GPa for both  $\text{Co}_4\text{Sb}_{12}$  and  $\text{In}_{0.1}\text{Co}_4\text{Sb}_{12}$  [52]. Hardness was determined in units of GPa from the load in newtons and the impression diagonal ( $2a$ ) in millimeters by the following:

$$H = \alpha_o \frac{P}{(2a)^2} \quad (4)$$

where  $\alpha_o$  is a numerical constant equal to 0.0018544 [53].

The crack-tip opening displacements (COD) technique was used to determine the intrinsic crack-tip toughness ( $K_{tip}$ ) from the Vickers indent cracks. Unlike the traditional measurement of fracture toughness,  $K_{tip}$  represents the intrinsic resistance of the material to crack propagation independent of extrinsic effects such as crack bridging, transformation toughening, etc.  $K_{tip}$  may be determined from the Young's modulus, crack length, indentation dimensions, and half-width of the measured crack openings displacements ( $\delta_{meas}$ ) as a function of their position from the crack tip ( $x$ ) according to the following [35, 37, 40]:

$$\frac{\delta}{K_{tip}} = \frac{\sqrt{a}}{E} \left( \sqrt{\frac{8}{\pi} \frac{x}{a}} + A_1 \left( \frac{x}{a} \right)^{1.5} + A_2 \left( \frac{x}{a} \right)^{2.5} \right) \quad (5a)$$

$$A_1 \cong 11.7 \exp \left[ -2.063 \left( \frac{c}{a} - 1 \right)^{0.28} \right] - \frac{0.898}{\frac{c}{a} - 1} \quad (5b)$$

$$A_2 \cong 44.5 \exp \left[ -3.712 \left( \frac{c}{a} - 1 \right)^{0.28} \right] - \frac{1}{\left( \frac{c}{a} - 1 \right)^{1.5}} \quad (5c)$$

Full crack openings displacements ( $2\delta_{meas}$ ) values were measured in a Quanta 600F SEM at 30 kV accelerating voltage using secondary electron imaging which gives a maximum resolution of  $\sim 1$  nm. Roughly 2 to 4 measurements were taken per micrometer of crack length and Fig. 1 shows several typical measurements over a few micrometers. According to the procedure outlined in [37],  $\delta_{calc}$  was calculated using Eq. 5 with the variable  $K_{tip}$  taken to be 1 MPa $\sqrt{\text{m}}$ . The data from four indents per composition were then plotted together, where the  $x$  and  $y$  components were  $\delta_{calc}$  and  $\delta_{meas}$ , respectively. Since  $K_{tip}$  is taken to be 1 MPa $\sqrt{\text{m}}$ , the magnitude of the slope of a linear fit to all the data reflects the ratio of  $\delta_{meas}$  to  $\delta_{calc}$ , and therefore, gives the intrinsic crack-tip toughness ( $K_{tip}$ ) of the material.

Finally, fracture toughness was determined on  $3 \times 4 \times 25\text{-}31 \text{ mm}^3$  micronotched specimens loaded in 4-point flexure using the single edge vee-notch bend (SEVNB) technique [30, 42-46]. Specimens were cut from the 40 mm hot-pressed samples with a low-speed water-cooled diamond saw and polished. Pre-notch cuts were made with a 0.2 mm kerf diamond blade. Razor micronotches were cut using 1  $\mu\text{m}$  diamond paste and repeatedly sliding a razor blade loaded with  $\sim 3 - 5 \text{ N}$  through the saw-cut notch in a custom-made jig. The resulting micronotch root radii were below 10  $\mu\text{m}$  as recommended in the literature [43-46]. The ratio of total notch length ( $n$ ) to specimen width ( $W$ ) was held constant for all specimens at  $\sim 0.3$ . The micronotched specimens were loaded in 4-point flexure in a BOSE EnduraTec ELF 3200 electromagnetic actuated load frame using a constant displacement rate of  $0.5 \text{ mm(min)}^{-1}$ . Fracture toughness was determined from the maximum load at fracture ( $P_f$ ), span ( $s = 6.47 \text{ mm}$ ), total notch length ( $n$ ), and specimen thickness and width ( $B$  and  $W$ ) [43]:

$$K_{IC} = \left( \frac{P_f s}{BW^{1.5}} \right) \left[ 1.5 \left( \frac{n}{W} \right)^{1.5} (Y) \right] \quad (6a)$$

$$\text{where } Y = \frac{1.99 - \left( \frac{n}{W} \right) \left[ 1 - \left( \frac{n}{W} \right) \right] \left[ 2.15 - 3.93 \left( \frac{n}{W} \right) + 2.7 \left( \frac{n}{W} \right)^2 \right]}{\left[ 1 - 2 \left( \frac{n}{W} \right) \right] \left[ 1 - \left( \frac{n}{W} \right) \right]^{1.5}} \quad (6b)$$

The resulting fracture surfaces were analyzed using a Quanta 600F SEM. Samples were fixed to sample holders using AquaDAG<sup>©</sup> and analyzed at a working distance of 10 mm.

When possible, student's t-tests were used to compare the mean fracture toughness values of the two compositions with  $p < 0.05$  considered statistically significant.

### 3. Results

#### 3.1 Crystal Structure and Microstructure

Powder X-ray diffraction data reveal both samples crystallize in a body-centered cubic IM-3 space group with the skutterudite crystal structure (Fig. 2). No impurity is discernible from the diffraction data. A slight increase in lattice parameter is observed in the doped  $\text{In}_{0.1}\text{Co}_4\text{Sb}_{12}$  sample (Fig. 2). Average grain size of the 12 mm  $\text{Co}_4\text{Sb}_{12}$  and  $\text{In}_{0.1}\text{Co}_4\text{Sb}_{12}$  hot pressed samples (Fig. 3) were quite different and measured to be estimated to be 1-2 and 15-40  $\mu\text{m}$ , respectively, using the intercept method [50, 51]. The large range in the latter case is reflective of small isolated grains being present in a large grained microstructure (Fig. 3b). For the 40 mm hot pressed samples both compositions had the same average grain size of 15  $\mu\text{m}$  making the direct comparison of mechanical properties easier.

### 3.2 Thermoelectric Properties

Both pure  $\text{Co}_4\text{Sb}_{12}$  12 mm and 40 mm samples are semiconducting, while both indium-doped  $\text{In}_{0.1}\text{Co}_4\text{Sb}_{12}$  compositions exhibit degenerate electrical conductivity – that is, the conductivity decreases with increasing temperature (Fig. 4a). The electrical conductivity is enhanced significantly in the indium-doped  $\text{In}_{0.1}\text{Co}_4\text{Sb}_{12}$  compositions. In addition, the Seebeck coefficient data (Fig. 4b) of the pure  $\text{Co}_4\text{Sb}_{12}$  samples exhibit an S-like trend with increasing temperature – typical of cobalt antimonide skutterudites with an anion deficiency [54]; while the Seebeck coefficient data of indium-doped  $\text{In}_{0.1}\text{Co}_4\text{Sb}_{12}$  samples is relatively stable with increasing temperature – typical of other reported indium-doped skutterudites [12, 47, 55]. Consequently, the power factor ( $\sigma S^2$ ) is enhanced dramatically upon indium doping (Fig. 5a). The thermal conductivities of the 12 mm samples are shown (Fig. 5b) and it is seen that the thermal conductivity of the indium-filled sample is suppressed relative to the pure  $\text{Co}_4\text{Sb}_{12}$  (Fig. 5b). Accordingly, the dimensionless thermoelectric figure-of-merit (ZT) is substantially improved upon indium doping (Fig. 6).

### 3.3 Fracture Toughness

Average  $\pm$  standard deviation hardness values of  $\text{Co}_4\text{Sb}_{12}$  and  $\text{In}_{0.1}\text{Co}_4\text{Sb}_{12}$  were  $H = 3.35 \pm 0.29$  and  $6.10 \pm 0.60$  GPa, respectively, as derived from the indent dimensions and Eq. 4. The results of the VIF tests revealed an apparent significant difference in fracture toughness is observed between the two 12 mm samples. It was found that the finer-grained  $\text{Co}_4\text{Sb}_{12}$  sample appeared to have nearly twice the fracture toughness of the  $\text{In}_{0.1}\text{Co}_4\text{Sb}_{12}$  sample with mean  $\pm$  standard deviation calculated using Eq. 3 as  $0.82 \pm 0.11$  versus  $0.46 \pm 0.13$  MPa $\sqrt{\text{m}}$ , respectively. It should be noted that spalling due to lateral crack formation was a significant problem for the  $\text{In}_{0.1}\text{Co}_4\text{Sb}_{12}$  composition and, accordingly, it was necessary to use much lower indentation loads to get suitable indents for hardness measurements [53] and crack length measurements [26].

Results for  $K_{\text{tip}}$  using the COD technique are shown (Fig. 7).  $\delta_{\text{meas}}$  data from four cracks taken from multiple indents is plotted against  $\delta_{\text{calc}}$  (calculated according to Eq. 5). The slope of the linear fit of each data set gives nearly identical  $K_{\text{tip}}$  values of  $0.52 \pm 0.04$  and  $0.53 \pm 0.04$  MPa $\sqrt{\text{m}}$  for  $\text{Co}_4\text{Sb}_{12}$  and  $\text{In}_{0.1}\text{Co}_4\text{Sb}_{12}$ , respectively.

Fracture toughness values of  $0.51 \pm 0.06$  and  $0.57 \pm 0.06$  MPa $\sqrt{\text{m}}$  were calculated using Eq. 6 for  $\text{Co}_4\text{Sb}_{12}$  and  $\text{In}_{0.1}\text{Co}_4\text{Sb}_{12}$ , respectively, using the SEVNB fracture toughness tests using micronotched samples loaded in 4-point flexure. No statistically significant difference

in  $K_{IC}$  ( $p = 0.89$ ) was found between the  $\text{Co}_4\text{Sb}_{12}$  and indium-filled  $\text{In}_{0.1}\text{Co}_4\text{Sb}_{12}$  compositions. Moreover, the values are similar to the intrinsic crack-tip toughness values found by assessing the crack opening displacements. Examination of the fracture surfaces of the SEVNB specimens revealed a primarily intergranular crack path for both compositions (Fig. 8). Finally, Table 1 summarizes the results for the three different methods.

#### 4. Discussion

##### 4.1 Crystal Structure and Microstructure

Lattice parameter expansion is a well-known response of most skutterudites to icosahedral void-site filling [3, 12, 13]. Accordingly, the observed lattice parameter expansion (Fig. 2) upon indium addition indicates that indium fills the icosahedral void-sites of the skutterudite crystal structure. The diffraction peaks of both  $\text{Co}_4\text{Sb}_{12}$  and  $\text{In}_{0.1}\text{Co}_4\text{Sb}_{12}$  are sharp, indicating high crystallinity in both samples. However, the microstructure of the hot-pressed 12 mm and 40 mm samples are quite different due to the shorter sintering time of the former (Fig. 3). The large differences in grain morphology observed in the 12 mm  $\text{Co}_4\text{Sb}_{12}$  and  $\text{In}_{0.1}\text{Co}_4\text{Sb}_{12}$  samples is likely due to a liquid-phase impurity (e.g. antimony or indium antimonide) present during sintering [56]. The 40 mm hot-pressed samples, however, both exhibit similar grain morphology. Well-defined triple points are apparent and the grain size distribution is quite narrow. Thus, the 40 mm hot-pressed samples provide a direct grain size independent comparison for determining the role of indium doping on the fracture toughness.

##### 4.2 Thermoelectric Properties

The dramatic increase in electrical conductivity (Fig. 4a) and the essentially temperature independent Seebeck coefficient behavior (Fig. 4b) exhibited by the indium-doped  $\text{In}_{0.1}\text{Co}_4\text{Sb}_{12}$  samples is further evidence that indium indeed fills the icosahedral void-sites of the skutterudite crystal structure as expected from the X-ray diffraction data. Moreover, the thermal conductivity of the indium-filled  $\text{In}_{0.1}\text{Co}_4\text{Sb}_{12}$  12 mm sample is significantly depressed compared to the  $\text{Co}_4\text{Sb}_{12}$  12 mm sample (Fig. 5b). Fig. 6 illustrates the importance of doping on the thermoelectric properties as the effects described above combine to produce a dramatic enhancement in ZT upon interstitial void-site doping with indium.

##### 4.3 Fracture Toughness

Spalling was a significant problem for the Vickers indentations for most of the microstructures examined with the exception of the finest grained 12 mm  $\text{Co}_4\text{Sb}_{12}$  samples.

Spalling is caused when a lateral crack system forms below the indent and the lateral cracks propagate to the free surface creating chips that separate from the bulk. Well defined indents without spalling were not obtained for the 40 mm samples at any indentation loads. For the 12 mm  $\text{In}_{0.1}\text{Co}_4\text{Sb}_{12}$  composition it was necessary to reduce the indent loads by roughly an order of magnitude (0.25 – 0.98 N) relative to the  $\text{Co}_4\text{Sb}_{12}$  composition (4.9 – 9.8 N) to avoid spalling and to get suitable indents for the hardness and  $K_c$  measurements [26, 53]. This made it impossible to measure those values for the two compositions at the same indentation loads since adequate crack lengths could not be achieved in  $\text{Co}_4\text{Sb}_{12}$  at low loads, and spalling occurred in  $\text{In}_{0.1}\text{Co}_4\text{Sb}_{12}$  at higher loads. The measured hardness varied by nearly a factor of two and follows the trend of the well-known indentation size effect where the measured hardness decreases with increasing indentation load [57]. Such a large effect on the hardness is not uncommon over the load range needed to get appropriate indents for these skutterudites [57]. Furthermore, this illustrates one of the major problems with assessing fracture toughness based on Eq. 3 where the hardness is one of the variables which affects the apparent fracture toughness value. Indeed, some of the apparent difference in the VIF toughness calculated for the two compositions (Table 1) can be explained by the difference in hardness from the indentation size effect.

In contrast, both the COD and SEVNB methods agreed that there was no difference in fracture toughness between the  $\text{Co}_4\text{Sb}_{12}$  and  $\text{In}_{0.1}\text{Co}_4\text{Sb}_{12}$  compositions for both the 12 mm and 40 mm samples, respectively (Table 1). This suggests that there is no embrittlement with interstitial doping with indium. While subsurface lateral cracking has been reported to cause errors in the COD method for one case with a SiC ceramic [58], the technique has generally proven to be quite robust and successful for a range of brittle materials including oxide glasses [35, 41],  $\text{Si}_3\text{N}_4$  ceramics [36, 37, 39], and lead zirconate titanate ferroelectric ceramics [38]. In the present study, the generally good agreement between the COD and SEVNB methods suggests the COD method can also be quite successful for brittle thermoelectric skutterudites. Conversely, a comparison of the fracture toughness values determined from all three techniques (Table 1) demonstrates that the VIF technique does not satisfactorily quantify fracture toughness in the skutterudite specimens as both SEVNB and COD techniques produced similar values. Although the VIF technique has been widely used for skutterudites [25], as has been pointed out in many previous studies the present results suggest the VIF technique should be avoided [27-34].

Despite the observed intergranular crack path (Fig. 8) which often promotes microstructure dependent extrinsic toughening in brittle materials via grain bridging in the

wake of the crack [59-62], the essentially identical results for the COD derived  $K_{tip}$  and the SEVNB derived  $K_{IC}$  suggest 1) fracture toughness did not depend on the grain size (Fig. 3) and 2) crack bridging is not a significant toughening mechanism for the present brittle skutterudites. The effect of grain bridging can be expressed as:

$$K_{IC} = K_{tip} - K_{br}, \quad K_{br} < 0 \quad (7)$$

where the negative value  $K_{br}$  is the result of contact across the crack wake that sustains some of the applied stress, thus raising the measured  $K_{IC}$ . Inserting the values from Table 1 into Eq. 7 shows that  $K_{br} \approx 0$  and there is no significant toughening by crack bridging in these materials. Accordingly, adjusting the composition or microstructure to promote crack bridging may be a good way to promote toughening in  $\text{Co}_4\text{Sb}_{12}$  based skutterudites.

The range of fracture toughness values found using the COD and SEVNB techniques (0.51 to 0.57 MPa $\sqrt{\text{m}}$ ) is much lower than the value of 1.7 MPa $\sqrt{\text{m}}$  previously reported for an n-type doped  $\text{Co}_4\text{Sb}_{12}$  based skutterudite using chevron notched bend specimens [24]. One possible explanation for the difference is that the doping and/or microstructure in that study promoted toughening by crack bridging giving a much higher  $K_{IC}$  value. However, in that study the authors noted an inconsistency in the results for a different skutterudite tested using both the SEVNB and chevron methods and they remarked more examination of the chevron notched method was needed. Thus, it is impossible to determine if the difference is the result is a true material property difference, or simply an artifact of the method used in [24]. Overall, the low toughness values measured in the present study stimulate genuine concern for the durability of future skutterudite-based thermoelectric modules.

## 5. Conclusions

Based on a study of the fracture toughness of undoped  $\text{Co}_4\text{Sb}_{12}$  and indium doped  $\text{In}_{0.1}\text{Co}_4\text{Sb}_{12}$  skutterudites using three different testing techniques, the following conclusions can be made:

1. The indium additions filled icosahedral void-sites as verified by an observed increase in the crystal lattice parameter and strongly enhanced thermoelectric properties in the indium-doped samples.
2. The fracture toughness of  $\text{Co}_4\text{Sb}_{12}$  and interstitially doped  $\text{In}_{0.1}\text{Co}_4\text{Sb}_{12}$  was found to be identical using both the crack tip opening displacement (COD) and single-edge vee-notched bend (SEVNB) methods indicating no interstitial embrittlement occurs due to indium void-site filling.

3. The intrinsic crack-tip toughness determined by the COD method was identical to the fracture toughness determined by the SEVNB tests indicating that there is no significant extrinsic toughening by crack bridging or other mechanisms and the toughness was insensitive to grain size variations.
4. Fracture toughness values derived from the Vickers indentation fracture (VIF) method did not agree with the other two methods. Numerous published studies have reported the VIF method to be inaccurate and have advised that the method should be avoided. Our results are in agreement with those assessments.
5. The results suggest the fracture toughness of skutterudites can be significantly lower than previously reported. While it is expected higher values can be achieved by different microstructures and/or compositions, the low toughness values for the presently reported materials ( $\sim 0.5 \text{ MPa}\sqrt{\text{m}}$ ) generates genuine concern over the durability of skutterudite-based power-producing thermoelectric modules if care is not taken to ensure adequate toughness.

## Acknowledgements

This research was supported by a grant from the National Science Foundation (DMR 0804167). J.E. would like to thank R. Berthelot for assistance with LeBail profile fitting.

## References

- [1] G.J. Snyder, E.S. Toberer, Complex thermoelectric materials, *Nat. Mater.*, 7 (2008) 105-114.
- [2] L.E. Bell, Cooling, heating, generating power, and recovering waste heat with thermoelectric systems, *Sci.*, 321 (2008) 1457-1461.
- [3] T.M. Tritt, M.A. Subramanian, Thermoelectric materials, phenomena, and applications: A bird's eye view, *MRS Bull.*, 31 (2006) 188-194.
- [4] D.M. Rowe, C.M. Bhandari, *Modern thermoelectrics*, 1983.
- [5] D.M. Rowe, *CRC handbook of thermoelectrics*, in, CRC Press, Boca Raton, FL, 1995.
- [6] G. Rogl, A. Grytsiv, N. Melnychenko-Koblyuk, E. Bauer, S. Laumann, P. Rogl, Compositional dependence of the thermoelectric properties of  $(\text{Sr}_x\text{Ba}_{1-x})_y\text{Co}(4)\text{Sb}(12)$  skutterudites, *J. Phys.: Condens. Matter*, 23 (2011).
- [7] J. Eilertsen, S. Rouvimov, M.A. Subramanian, Rattler-seeded InSb nanoinclusions from metastable indium-filled  $\text{In}_{0.1}\text{Co}_4\text{Sb}_{12}$  skutterudites for high-performance thermoelectrics, *Acta Mater.*, 60 (2012) 2178-2185.
- [8] J. Eilertsen, R. Berthelot, A.W. Sleight, M.A. Subramanian, Structure and transport behavior of In-filled cobalt rhodium antimonide skutterudites, *J. Solid State Chem.*, 190 (2012) 238-245.
- [9] G.S. Nolas, D.T. Morelli, T.M. Tritt, Skutterudites: A phonon-glass-electron crystal approach to advanced thermoelectric energy conversion applications, *Annu. Rev. Mater. Sci.*, 29 (1999) 89-116.

- [10] G.S. Nolas, H. Takizawa, T. Endo, H. Sellinschegg, D.C. Johnson, Thermoelectric properties of Sn-filled skutterudites, *Appl. Phys. Lett.*, 77 (2000) 52-54.
- [11] G.J. Long, B. Mahieu, B.C. Sales, R.P. Hermann, F. Grandjean, Electronic structure of thallium filled skutterudites studied by x-ray absorption and Mossbauer spectroscopy, *J. Appl. Phys.*, 92 (2002) 7236-7241.
- [12] T. He, J.Z. Chen, H.D. Rosenfeld, M.A. Subramanian, Thermoelectric properties of indium-filled skutterudites, *Chem. Mater.*, 18 (2006) 759-762.
- [13] J. Eilertsen, J. Li, S. Rouvimov, M.A. Subramanian, Thermoelectric properties of indium-filled  $In_xRh_4Sb_{12}$  skutterudites, *J. Alloys Compd.*, 509 (2011) 6289-6295.
- [14] Z. Xiong, X. Chen, X. Huang, S. Bai, L. Chen, High thermoelectric performance of  $Yb_{0.26}Co_4Sb_{12}/yGaSb$  nanocomposites originating from scattering electrons of low energy, *Acta Mater.*, 58 (2010) 3995-4002.
- [15] J.Y. Peng, P.N. Alboni, J. He, B. Zhang, Z. Su, T. Holgate, N. Gothard, T.M. Tritt, Thermoelectric properties of (In,Yb) double-filled  $CoSb_3$  skutterudite, *J. Appl. Phys.*, 104 (2008).
- [16] S. Lee, J.C.M. Li, C.T. Liu, Pinning of dislocations by solutes in NiAl, *Mater. Sci. Eng., A*, 239-240 (1997).
- [17] G. Duscher, M.F. Chisholm, U. Alber, M. Ruhle, Bismuth-induced embrittlement of copper grain boundaries, *Nat. Mater.*, 3 (2004) 621-626.
- [18] R.Q. Wu, A.J. Freeman, G.B. Olson, First principles determination of the effects of phosphorus and boron on iron grain-boundary cohesion, *Sci.*, 265 (1994) 376-380.
- [19] R.P. Messmer, C.L. Briant, The role of chemical bonding in grain-boundary embrittlement, *Acta Metall.*, 30 (1982) 457-467.
- [20] W. Losch, New model of grain-boundary failure in temper embrittled steel, *Acta Metall.*, 27 (1979) 1885-1892.
- [21] X. Shi, W. Zhang, L.D. Chen, J. Yang, Filling fraction limit for intrinsic voids in crystals: Doping in skutterudites, *Phys. Rev. Lett.*, 95 (2005).
- [22] Z. Xiong, L.L. Xi, J. Ding, X.H. Chen, X.Y. Huang, H. Gu, L.D. Chen, W.Q. Zhang, Thermoelectric nanocomposite from the metastable void filling in caged skutterudite, *J. Mater. Res.*, 26 (2011) 1848-1856.
- [23] D. Wee, B. Kozinsky, N. Marzari, M. Fornari, Effects of filling in  $CoSb_3$ : Local structure, band gap, and phonons from first principles, *Phys. Rev. B: Condens. Matter*, 81 (2010).
- [24] V. Ravi, S. Firdosy, T. Caillat, B. Lerch, A. Calamino, R. Pawlik, M. Nathal, A. Sechrist, J. Buchhalter, S. Nutt, Mechanical properties of thermoelectric skutterudites, in: M.S. ElGenk (Ed.) *Space Technology and Applications International Forum Staif 2008*, 2008, pp. 656-662.
- [25] G. Rogl, P. Rogl, Mechanical Properties of Skutterudites, *Sci. Adv. Mater.*, 3 (2011) 517-538.
- [26] G.R. Anstis, P. Chantikul, B.R. Lawn, D.B. Marshall, A critical evaluation of indentation techniques for measuring fracture toughness. I. Direct crack measurements, *J. Am. Ceram. Soc.*, 64 (1981) 533-538.
- [27] C.B. Ponton, R.D. Rawlings, Vickers indentation fracture toughness test. Part 2. Application and critical evaluation of standardized indentation toughness equations, *Mater. Sci. Technol.*, 5 (1989) 961-976.
- [28] C.B. Ponton, R.D. Rawlings, Vickers indentation fracture toughness test. Part 1. Review of literature and formulation of standardized indentation toughness equations, *Mater. Sci. Technol.*, 5 (1989) 865-872.
- [29] G.D. Quinn, R.C. Bradt, On the Vickers indentation fracture toughness test, *J. Am. Ceram. Soc.*, 90 (2007) 673-680.
- [30] R. Morrell, Fracture toughness testing for advanced technical ceramics: internationally agreed good practice, *Adv. Appl. Ceram.*, 105 (2006) 88-98.

- [31] J.J. Kruzic, D.K. Kim, K.J. Koester, R.O. Ritchie, Indentation techniques for evaluating the fracture toughness of biomaterials and hard tissues, *Journal of the Mechanical Behavior of Biomedical Materials*, 2 (2009) 384-395.
- [32] R.F. Cook, G.M. Pharr, Direct observation and analysis of indentation cracking in glasses and ceramics, *J. Am. Ceram. Soc.*, 73 (1990) 787-817.
- [33] Z. Li, A. Ghosh, A.S. Kobayashi, R.C. Bradt, Indentation fracture toughness of sintered silicon carbide in the Palmqvist crack regime, *J. Am. Ceram. Soc.*, 72 (1989) 904-911.
- [34] A. Ghosh, Z. Li, C.H. Henager Jr., A.S. Kobayashi, R.C. Bradt, Vickers microtoughness of SiC in the median-crack regime, in: R.C. Bradt, D.P.H. Hasselman, D. Munz, M. Sakai, V.Y. Shevchenko (Eds.) *Fracture Mechanics of Ceramics*, Plenum Press, New York, Karlsruhe, Germany, 1996, pp. 219-231.
- [35] T. Fett, A.B. Kounga Njiwa, J. Rödel, Crack opening displacements of Vickers indentation cracks, *Eng. Fract. Mech.*, 72 (2005) 647-659.
- [36] S. Fünfschilling, T. Fett, M. Hoffmann, R. Oberacker, H. Jelitto, G. Schneider, Determination of the crack-tip toughness in silicon nitride ceramics, *J. Mater. Sci.*, 44 (2009) 335-338.
- [37] S. Fünfschilling, T. Fett, R. Oberacker, M.J. Hoffmann, G.A. Schneider, P.F. Becher, J.J. Kruzic, Crack- tip toughness from Vickers crack-tip opening displacements for materials with strongly rising R- curves, *J. Am. Ceram. Soc.*, 94 (2011) 1884-1892.
- [38] A.B. Kounga Njiwa, T. Fett, D.C. Lupascu, J. Rödel, Crack-tip toughness of a soft lead zirconate titanate, *J. Am. Ceram. Soc.*, 86 (2003) 1973-1975.
- [39] A.B. Kounga Njiwa, T. Fett, J. Rödel, G.D. Quinn, Crack-tip toughness measurements on a sintered reaction-bonded  $\text{Si}_3\text{N}_4$ , *J. Am. Ceram. Soc.*, 87 (2004) 1502-1508.
- [40] G.A. Schneider, T. Fett, Computation of the stress intensity factor and COD for submicron sized indentation cracks, *J. Ceram. Soc. Jpn.*, 114 (2006) 1044-1048.
- [41] Z. Burghard, A. Zimmermann, J. Rödel, F. Aldinger, B.R. Lawn, Crack opening profiles of indentation cracks in normal and anomalous glasses, *Acta Mater.*, 52 (2004) 293-297.
- [42] D. Munz, R.T. Bubsey, J.L. Shannon Jr., Fracture toughness determination of  $\text{Al}_2\text{O}_3$  using four-point-bend specimens with straight-through and chevron notches, *J. Am. Ceram. Soc.*, 63 (1980) 300-305.
- [43] T. Nishida, Y. Hanaki, G. Pezzotti, Effect of notch-root radius on the fracture toughness of a fine-grained alumina, *J. Am. Ceram. Soc.*, 77 (1994) 606-608.
- [44] C.V. Rocha, C.A. da Costa, Effect of notch-root radius on the fracture toughness of composite  $\text{Si}_3\text{N}_4$  ceramics, *Journal of Materials Engineering and Performance*, 15 (2006) 591-595.
- [45] F.H. Wang, Prediction of intrinsic fracture toughness for brittle materials from the apparent toughness of notched-crack specimen, *J. Mater. Sci.*, 35 (2000) 2543-2546.
- [46] R. Damani, R. Gstrein, R. Danzer, Critical notch-root radius effect in SENB-S fracture toughness testing, *J. Eur. Ceram. Soc.*, 16 (1996) 695-702.
- [47] A. Sesselmann, T. Dasgupta, K. Kelm, E. Mueller, S. Perlt, S. Zastrow, Transport properties and microstructure of indium-added cobalt-antimony-based skutterudites, *J. Mater. Res.*, 26 (2011) 1820-1826.
- [48] A. Lebail, H. Duroy, J.L. Fourquet, Ab initio structure determination of  $\text{LiSbWO}_6$  by X-ray powder diffraction, *Mater. Res. Bull.*, 23 (1988) 447-452.
- [49] J. Rodríguez-Carvajal, Recent advances in magnetic structure determination by neutron powder diffraction, *Physica B*, 192 (1993) 55-69.
- [50] J. Hilliard, Estimating Grain Size by the Intercept Method, *Metal Prog.*, 85 (1964).
- [51] ASTM Standard E112, 2012, Standard Test Methods for Determining Average Grain Size, in, ASTM International, West Conshohocken, Pennsylvania, USA, 2010, pp. DOI: 10.1520/E0112-1510, <http://www.astm.org>.

- [52] K. Biswas, M.S. Good, K.C. Roberts, M.A. Subramanian, T.J. Hendricks, Thermoelectric and structural properties of high-performance In-based skutterudites for high-temperature energy recovery, *J. Mater. Res.*, 26 (2011) 1827-1835.
- [53] ASTM Standard C1327, 2008, Standard Test Method for Vickers Indentation Hardness of Advanced Ceramics, in, ASTM International, West Conshohocken, Pennsylvania, USA, 2008, pp. DOI: 10.1520/C1327-1508, <http://www.astm.org>.
- [54] C.-H. Park, Y.-S. Kim, Ab initio study of native point-defects in CoSb<sub>3</sub>: Understanding off-stoichiometric doping properties, *Phys. Rev. B: Condens. Matter*, 81 (2010).
- [55] K. Akai, H. Kurisu, T. Moriyama, S. Yamamoto, M. Matsuura, I. Ieee, Effects of defects and impurities on electronic properties in skutterudites, 1998.
- [56] W.S. Liu, B.P. Zhang, J.F. Li, L.D. Zhao, Effects of Sb compensation on microstructure, thermoelectric properties and point defect of CoSb<sub>3</sub> compound, *J. Phys. D-Appl. Phys.*, 40 (2007) 6784-6790.
- [57] J.B. Quinn, G.D. Quinn, Indentation brittleness of ceramics: a fresh approach, *J. Mater. Sci.*, 32 (1997) 4331-4346.
- [58] J.J. Kruzic, R.O. Ritchie, Determining the toughness of ceramics from Vickers indentations using the crack-opening displacements: An experimental study, *J. Am. Ceram. Soc.*, 86 (2003) 1433-1436.
- [59] Y.-W. Mai, B.R. Lawn, Crack-interface grain bridging as a fracture resistance mechanism in ceramics: II, Theoretical fracture mechanics model, *J. Am. Ceram. Soc.*, 70 (1987) 289-294.
- [60] P.L. Swanson, C.J. Fairbanks, B.R. Lawn, Y.-W. Mai, B.J. Hockey, Crack-interface grain bridging as a fracture resistance mechanism in ceramics: I, Experimental study on alumina, *J. Am. Ceram. Soc.*, 70 (1987) 279-289.
- [61] J. Rödel, Crack closure forces in ceramics: Characterization and formation, *J. Eur. Ceram. Soc.*, 9 (1992) 323-334.
- [62] J. Rödel, J.F. Kelly, B.R. Lawn, In situ measurements of bridged crack interfaces in the scanning electron microscope, *J. Am. Ceram. Soc.*, 73 (1990) 3313-3318.

Table 1: Fracture toughness data summary showing mean  $\pm$  standard deviation

<b>Composition</b>	<b>VIF Toughness, <math>K_c</math></b>	<b>COD Toughness, <math>K_{tip}</math></b>	<b>SEVNB Toughness, <math>K_{IC}</math></b>
Co <sub>4</sub> Sb <sub>12</sub>	0.82 $\pm$ 0.11 MPa $\sqrt{m}$	0.52 $\pm$ 0.04 MPa $\sqrt{m}$	0.51 $\pm$ 0.06 MPa $\sqrt{m}$
In <sub>0.1</sub> Co <sub>4</sub> Sb <sub>12</sub>	0.46 $\pm$ 0.13 MPa $\sqrt{m}$	0.53 $\pm$ 0.04 MPa $\sqrt{m}$	0.57 $\pm$ 0.06 MPa $\sqrt{m}$

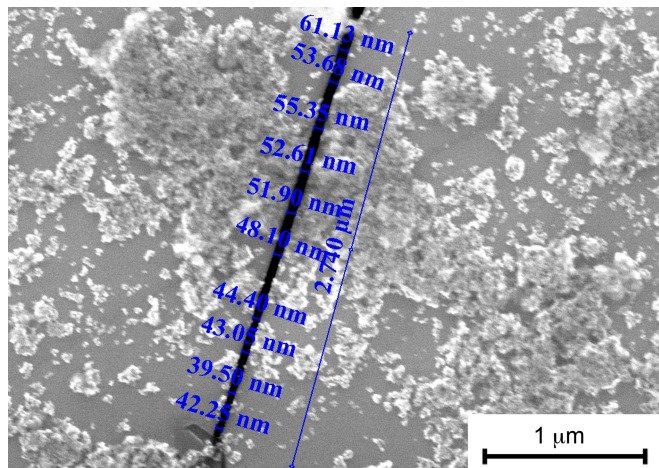


Figure 1: Example SEM micrograph showing full crack opening displacement ( $2\delta_{meas}$ ) measurements taken over a few micrometers of crack length.

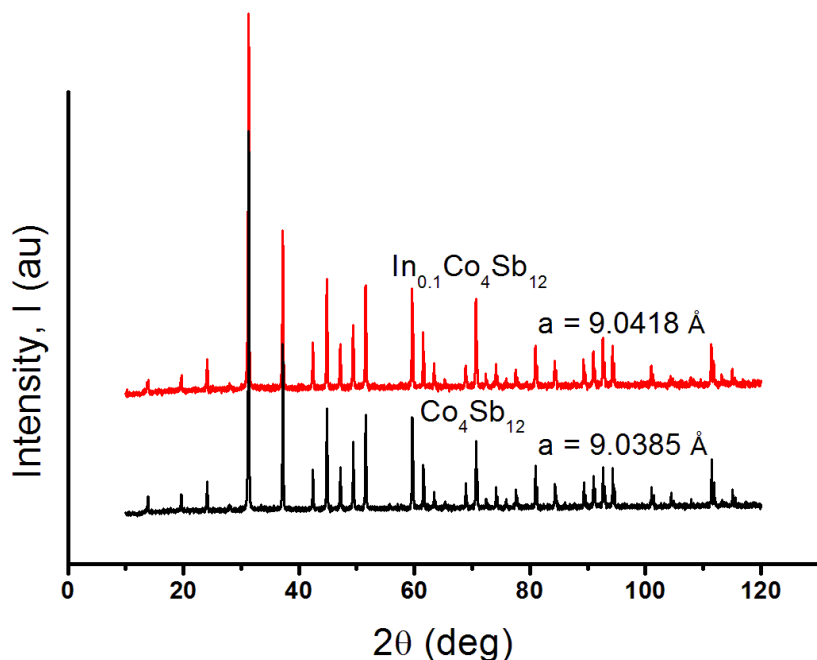


Figure 2: X-ray diffraction data of pure and interstitially doped skutterudites. Both samples are single phase. The lattice parameters of  $\text{Co}_4\text{Sb}_{12}$  and  $\text{In}_{0.1}\text{Co}_4\text{Sb}_{12}$  are shown. A slight expansion in lattice parameter is observed upon indium void-site filling. The  $a$  parameters derived from LeBail profile matching are known to  $10^{-5}$  nm.

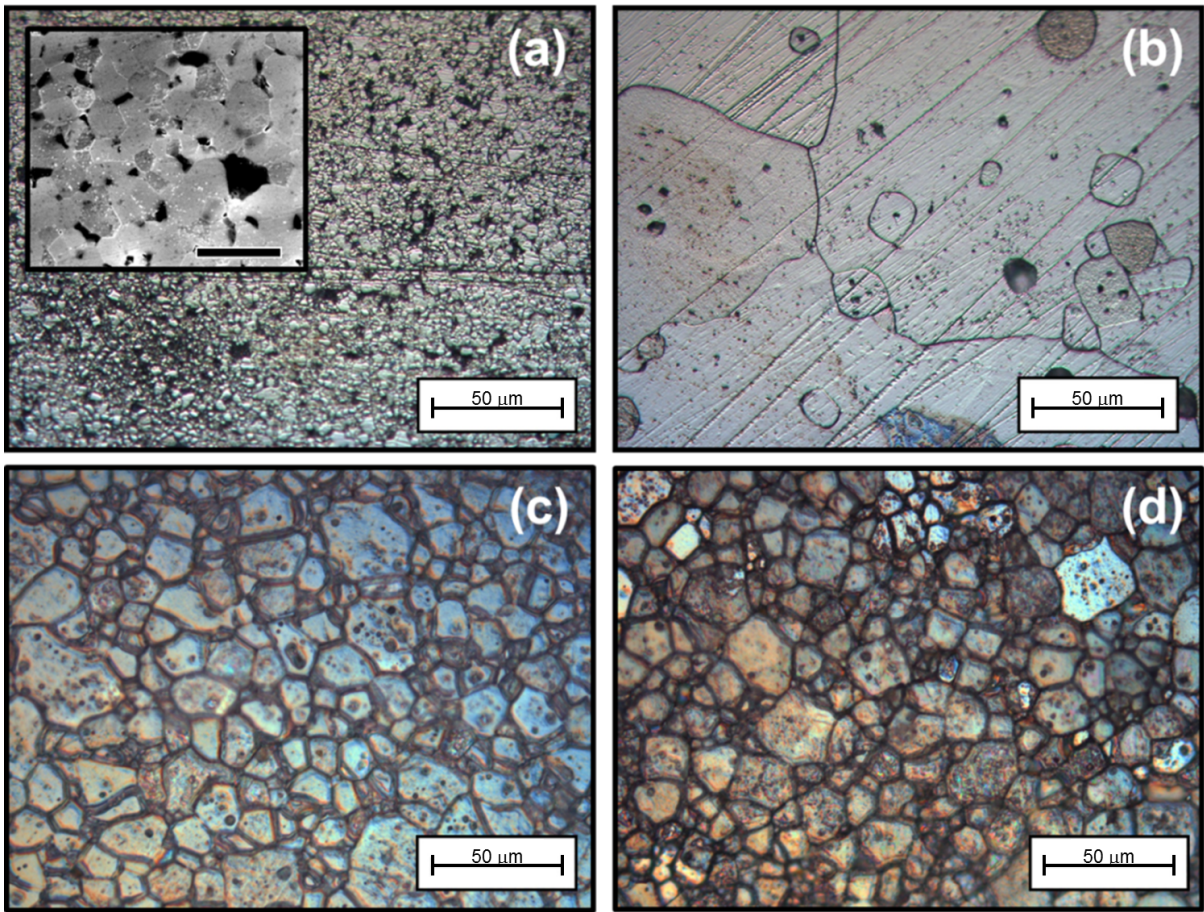


Figure 3: Microstructure of pure and interstitially doped skutterudites. The microstructure of the 12 mm (a, b) and 40 mm (c, d) Co<sub>4</sub>Sb<sub>12</sub> and In<sub>0.1</sub>Co<sub>4</sub>Sb<sub>12</sub> pellets, respectively. The calibration bar in the inset SEM image is 4 micrometers. The average grain diameters were determined from the Hilliard method and found to be 1-2  $\mu\text{m}$  (a), 15-40  $\mu\text{m}$  (b), 15  $\mu\text{m}$  (c), and 15  $\mu\text{m}$  (d). Note the distinctly bimodal microstructure of (b).

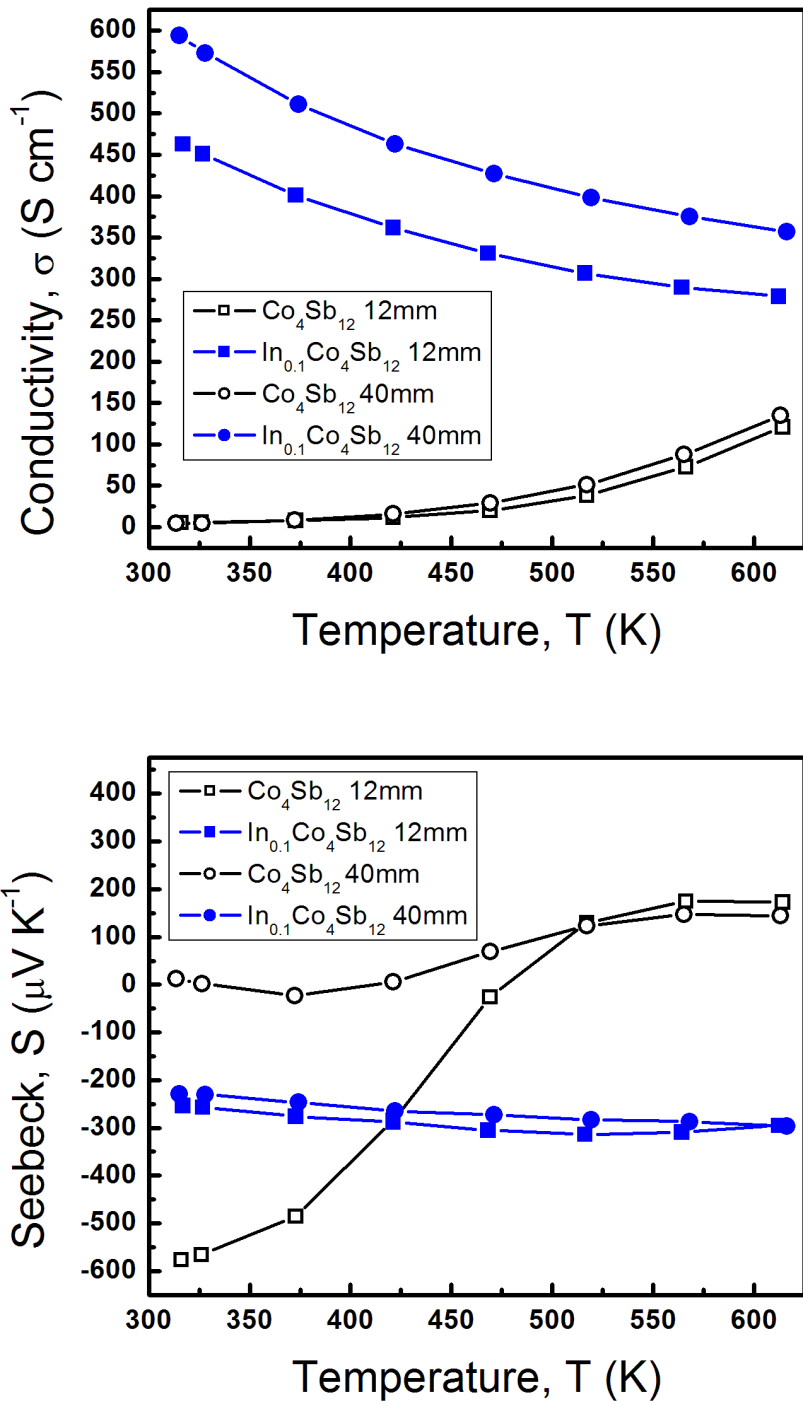


Figure 4: (a) Electrical conductivity of pure and interstitially doped skutterudites. The pure Co<sub>4</sub>Sb<sub>12</sub> samples are semiconducting, while the indium-filled In<sub>0.1</sub>Co<sub>4</sub>Sb<sub>12</sub> cobalt antimonide samples are degenerate. The electrical conductivity increases dramatically upon indium doping – typical of interstitially doped skutterudites. b) Seebeck coefficient data of pure and interstitially doped skutterudites showing the dramatic effect of indium doping. The S-like trend with temperature observed in the pure Co<sub>4</sub>Sb<sub>12</sub> samples is attributed to an anion deficiency.

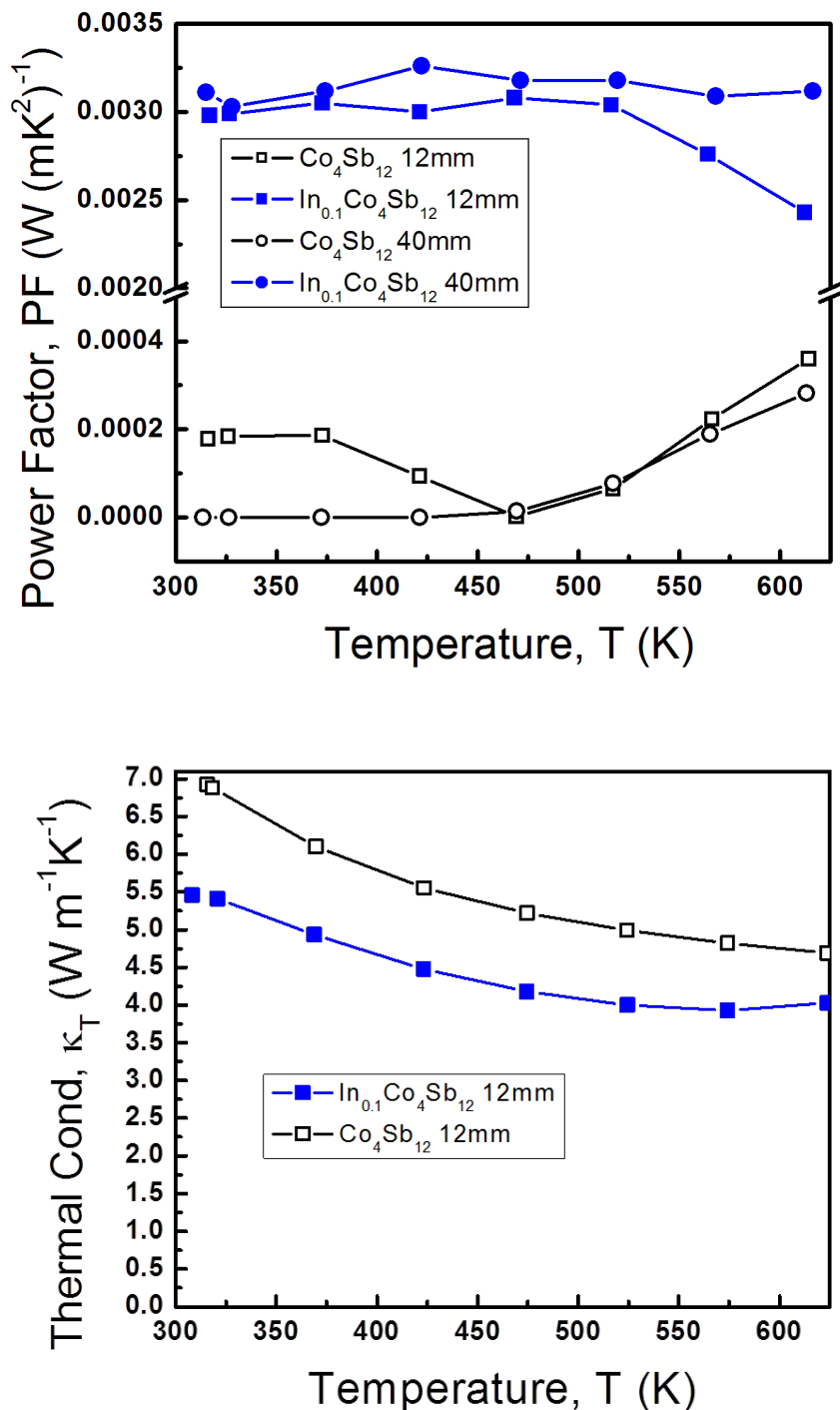


Figure 5: (a) Power factor of pure and interstitially doped skutterudites. The power factor is increased dramatically with indium additions. Note the scale-breaks in the y-axis. (b) Thermal conductivity of  $\text{Co}_4\text{Sb}_{12}$  and  $\text{In}_{0.1}\text{Co}_4\text{Sb}_{12}$  12 mm pellets. The thermal conductivity is suppressed with interstitial doping.

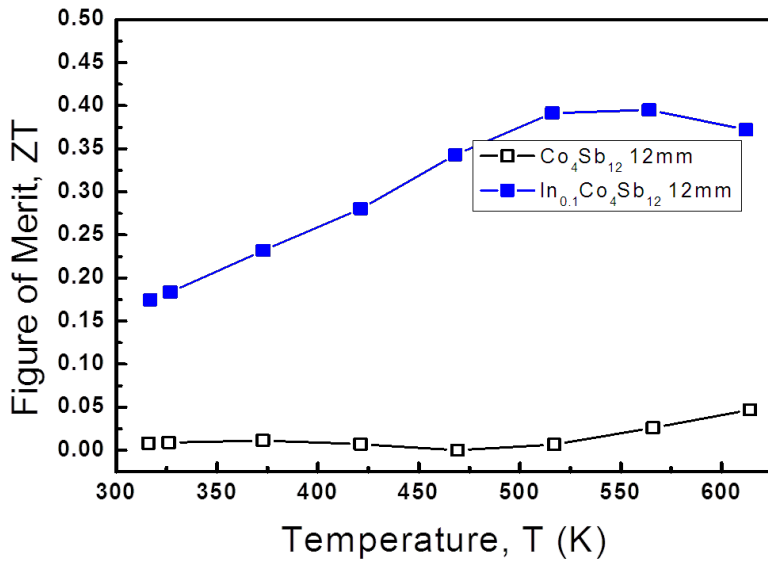


Figure 6: ZT data of  $\text{Co}_4\text{Sb}_{12}$  and  $\text{In}_{0.1}\text{Co}_4\text{Sb}_{12}$  12 mm pellets. The ZT of the interstitially doped sample is dramatically increased; consequently, only interstitially doped skutterudites can be used in high-efficiency thermoelectric modules.

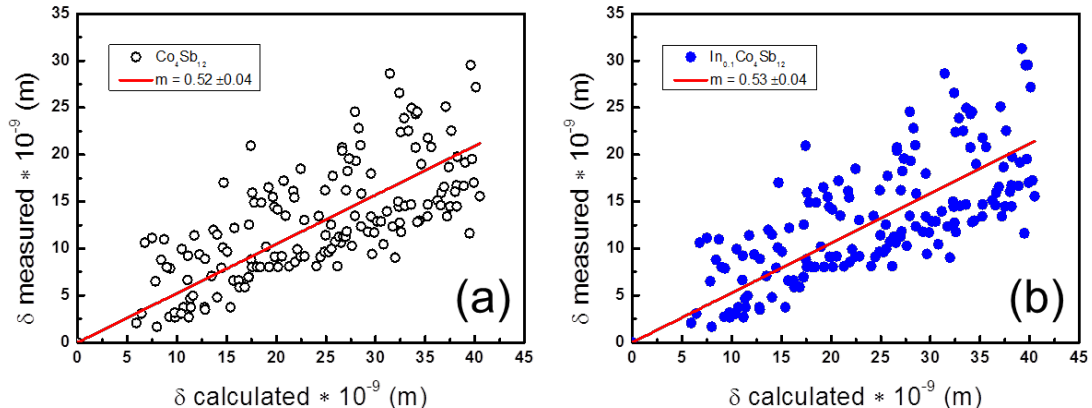


Figure 7: Intrinsic crack-tip toughness data. Four cracks of each sample were analyzed. The slopes of the linear fits give the intrinsic crack-tip toughness values of the  $\text{Co}_4\text{Sb}_{12}$  and  $\text{In}_{0.1}\text{Co}_4\text{Sb}_{12}$  samples. Both materials have the same intrinsic crack-tip toughness.

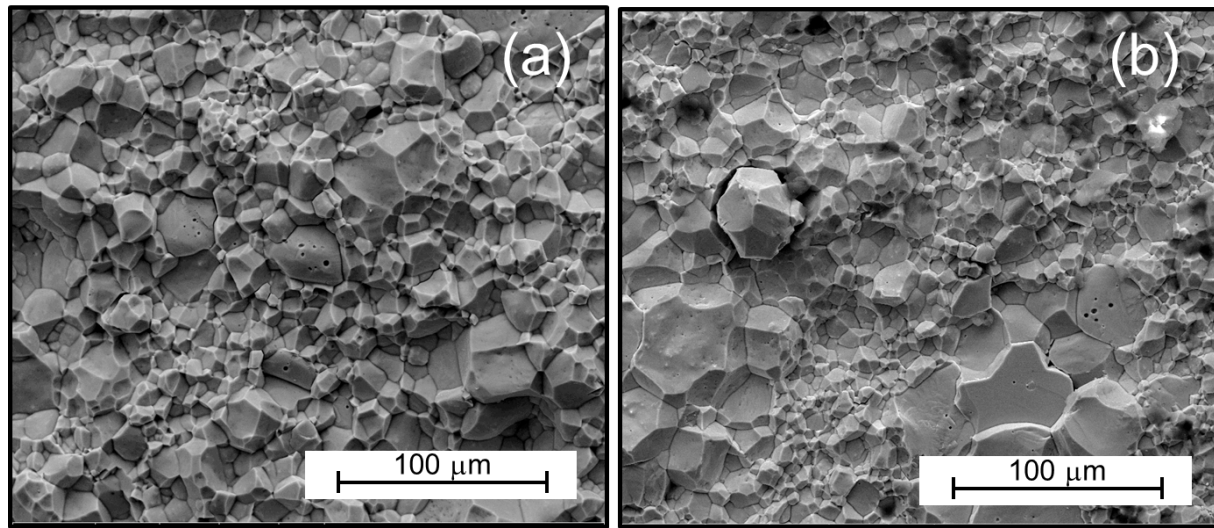


Figure 8: Fracture surface of the Co<sub>4</sub>Sb<sub>12</sub> (a) and In<sub>0.1</sub>Co<sub>4</sub>Sb<sub>12</sub> (b) SEVNB specimens. A primarily intergranular crack path was observed for both compositions.